Thrust scaling for a large-amplitude heaving and pitching foil with application to cycloidal propulsion

Jérémie Labasse[a], Uwe Ehrenstein[a,*], Guillaume Fasse[b], Frédéric Hauville[b]

[a] *Aix-Marseille Univ, CNRS, Centrale Marseille, M2P2, Marseille, France*
[b] *Naval Academy Research Institute (IRENav), BCMR Brest, CC600, 29240 Brest Cedex9, France*

Abstract

A numerical solution procedure using the mesh-superposition approach, known as the Chimera method, together with the OpenFOAM toolbox environment is used to compute the forces generated by large amplitude heaving and pitching foil. The possibility of fitting thrust prediction laws, based on classical potential flow theories, with the numerically computed forces is explored, for a Reynolds number of $5\ 10^4$. It is shown, first for a pure heaving motion and subsequently by adding a harmonic pitching motion, that theoretical scaling may be fitted to numerical time-averaged thrust data, even in the case of large amplitude motions. The thrust-prediction law is shown to still apply to pitching-rotating motions, such as those of blades in cycloidal propulsion devices, the mean pressure correction due to the additional surging motion being small. The synchronized rotation-pitching of three foils typical of a cross-flow propeller configuration is addressed as well. The numerical global thrust results are shown to be in general agreement with the theoretical prediction, but also with blade-embedded load cell measurements for an experimental device developed by the French Naval Academy Research Institute.

Keywords: Pitching and heaving foil; Thrust; Chimera method; Cycloidal propulsion

1. Introduction

Oscillating bodies in moving fluids are intimately related to swimming and flying and the question of thrust performance in this context has received considerable attention in the literature [1]. Pitching and heaving motions are

*Corresponding author
Email address: uwe.ehrenstein@univ-amu.fr (Uwe Ehrenstein)

often considered as archetypes of aquatic locomotion and it is the reason why they have widely been considered for thrust scaling investigations. It has been recognized that flapping wings' performance may be inferred from the wake structure of the wings, which exhibits in the case of thrust production jet-like average velocity profiles, associated with a reversed Kármán vortex street [2]. Applying for instance the integral momentum theory to a control volume in which the oscillating body is embedded, the generated thrust can be predicted by velocity measurements in the wake [3, 4], the reliability of this approach having been recently addressed in [5, 6], comparing measurements with numerical simulation results.

Theoretical models for thrust prediction based on potential flow theory have been proposed since the seminal work by Garrick [7], for swimming plates in [8] and more recently for example in [9, 10]. The formulas derived in [7] have been compared with numerical thrust force results, see for example [11–13], as well as with direct measurements (e.g. [14]). Scaling laws for pitching and heaving foils have also been compared with experimental data in [15, 16], among others. But despite the numerous numerical and experimental investigations on the hydrodynamics of flapping foils available (see [17] for a recent review), there is no general consensus about thrust models, in particular when moderate or large flapping amplitudes are required, as for example in the field of renewable power generation [18] and naval propulsion [19]. Indeed, large-amplitude oscillations of foils appear to be necessary to achieve efficient thrust magnitudes (e.g. [20]). The blades of a cycloidal propeller for instance undergo large-amplitude pitching-rotating motions and the associate performance of such devices has been addressed numerically in [21], while a low-order hydrodynamic model has been proposed and experimentally validated in [22]. Cycloidal fluid flow engines are also designed for tidal energy conversion and a Darrieu-type cross flow turbine has for instance been addressed in [23].

Concerning scaling laws, there have been attempts (see e.g. [24]) to extent the linear potential theory to foils undergoing large amplitude oscillations, experimental results having been compared with linear and nonlinear theory [15]. In [25], scaling relations have been proposed in particular for heaving amplitudes of the order of magnitude of the foil's chord.

When addressing numerically large amplitude oscillations of a foil, a key issue is to efficiently update the computational mesh. An alternative which has become widely used is to immerse the moving geometry on a simple Cartesian grid using more or less ad hoc momentum sources to model the kinematic condition at the interface between the velocity field and the body's moving boundary. This approach is known as the immersed boundary method and goes back to Peskin's seminal work [26]. Even though this approach may be

used for different Navier-Stokes discretization procedures as well as all types of structures (see e.g. [27, 28]), a difficulty associated with this method is however to accurately resolve the very vicinity of the body surface, in particular in the case of thin structures [29].
When large amplitude motions are addressed, the so-called overset grid approach, also known as the Chimera method, appears to be particularly appropriate as a body-fitted discretization procedure. The idea is to superimpose moving subdomains to a fixed meshed background global computational domain. The independently moving domains contain the structures in motion and the communication with the fixed mesh is achieved through interpolation within transmission zones. This method has first been documented in [30] and more recent analyses are given in [31–34], for instance. The open-source OpenFOAM toolbox has become very popular in academic research [35–37] as well as industrial flow simulations [38, 39], the Chimera-type approach having been implemented in several version of this numerical simulation environment and in particular in [40] (for a description of the overset-option, see for instance [41]).
The OpenFOAM toolbox and the overset-option is used in the present investigation, addressing the question of thrust-scaling for a large amplitude heaving foil as well as for a heaving-pitching foil. Heaving, pitching and surging are the three motions into which the displacement of pitching foils in cross-flow propellers can be decomposed. Considering such a propeller, which is part of an academic experimental project at the French Naval Academy Research Institute (IRENav) [42], simulations are performed for rotating-pitching foils for parameters close to those in the experiment.
The paper is organized as follows. A heaving foil is addressed in Section 2 using the OpenFOAM simulation environment, the numerical procedure using the overset-approach being presented and the numerical convergence is assessed as well. The forces generated by the foil's motion are computed for a large set of heaving parameters, allowing a successful fit with a thrust scaling law. Subsequently in Section 3 a pitching motion is added to heaving, the aim being again to propose a thrust prediction law, as function of the parameters. In Section 4 the foil's motion is made more complex adding a surging back-and-forth movement, such as to mimic motions in cross-flow propeller devices. In particular, the reliability of a mere heaving-pitching thrust law in this context is examined. Finally, dynamic force computations are compared with experimental measurements for the cycloidal propulsion device described in [42]. The results are discussed in the concluding Section 5.

2. Heaving foil

We consider a foil with chord L in a two-dimensional domain (x, y) immersed in an incoming incompressible flow of velocity U_∞, heaving in the direction normal to the incoming flow direction, the heaving motion being

$$h = h_0 L \sin(2\pi f t) \tag{1}$$

with h_0 the (dimensionless) ratio between the heaving amplitude and the chord, f being the heaving frequency. The heaving velocity is written $\dot{h}$ and the forces exerted on the foil are equivalent to those that would experience a fixed foil immersed in a flow with an angle of attack α and relative flow velocity U such that (see also [25])

$$\alpha = \arctan\left(\frac{-\dot{h}}{U_\infty}\right), \quad U = \sqrt{U_\infty^2 + \dot{h}^2}. \tag{2}$$

The foil therefore is subject to a lift force f_l as well as a form drag f_d respectively in the direction $\mathbf{e}_l$ and $\mathbf{e}_d$, forming en angle α with the streamwise x-direction, as sketched in figure 1. In the forthcoming analysis the flow quantities are made dimensionless with the foil's chord L and the incoming uniform flow velocity U_∞. Also, the convention will be used that thrust is positive and drag negative.
In the following, we consider what is known as the reduced frequency

$$k = \frac{\pi f L}{U_\infty} \tag{3}$$

as dimensionless quantity and accordingly the dimensionless heaving law is

$$h^* = h/L = h_0 \sin(2kt^*) \quad \text{and} \quad \dot{h}/U_\infty = 2kh_0 \cos(2kt^*). \tag{4}$$

with $t^* = tU_\infty/L$ the time made dimensionless. Accordingly, the angle of attack due to the heaving velocity can be written

$$\alpha = \arctan\left(-2kh_0 \cos(2kt^*)\right). \tag{5}$$

Here dimensionless frequencies and heaving amplitudes up to the order of one are to be considered which means that the time-varying angle of attack as experienced by the foil may be as large as $\pm 60°$. Reliable lift formula are however only known for relatively small angles of attack in the limit of inviscid flow, the lift force for a slender symmetrical body being known to be approximately $\pi \sin(\alpha) U^2 L \rho$ ([43]) with U the incoming flow. Of course,

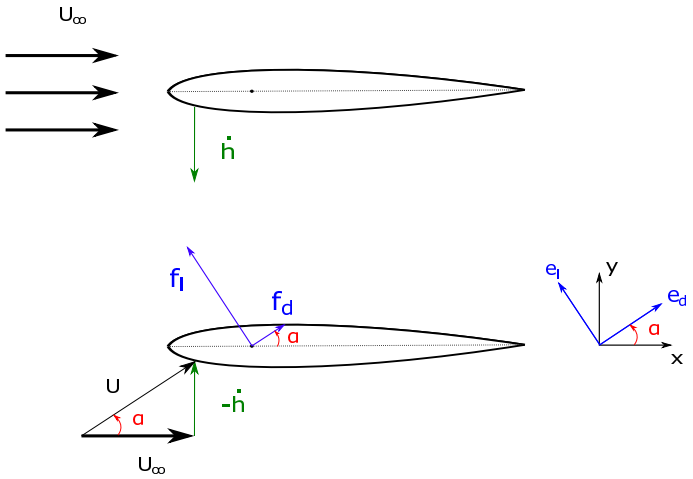


Figure 1: Sketch of the heaving foil immersed in an incoming flow: lower figure shows $\mathbf{U}$ as seen in the foil's coordinate system as well as the sketch of the lift $\mathbf{f}_l$ and the form drag $\mathbf{f}_d$.

there is no reason that such a formula quantitatively applies to the present heaving foil at large amplitudes. Considering nevertheless tentatively this formula (which would correspond to instantaneous lift f_l for varying α in the $\mathbf{e}_l$ direction as sketched in figure 1), its projection on the x-axis yields (with the convention that thrust is positive) $\pi \sin^2(\alpha) U^2 L \rho$, U being given by (2). According to (5)

$$\sin^2(\alpha) = \frac{4k^2h_0^2\cos^2(2kt^*)}{1+4k^2h_0^2\cos^2(2kt^*)} \quad \text{while} \quad U^2/U_\infty^2 = 1+4k^2h_0^2\cos^2(2kt^*) \tag{6}$$

and introducing a hypothetical proportionality factor C, a possible lift-induced dynamic thrust formula could be

$$f^*_{thrust} = C\ 4\pi k^2 h_0^2 \cos^2(2kt^*). \tag{7}$$

While uncountable data are of course available for drag coefficients as function of angles of attack for NACA foils, it seems however that general analytic drag laws are not available, besides the evidence that pressure drag increases with the angle of attack. Making the ad-hoc assumption in the present case that the time-dependent drag is qualitatively proportional to $|\sin(\alpha)| U^2 L \rho$, then the (dimensionless) drag in the $\mathbf{e}_d$ direction (see figure 1) would vary as

$$D\, 2k\, h_0\, |\cos(2kt^*)\,| \sqrt{1+4k^2h_0^2\cos^2(2kt^*)},$$

given (6), D being a hypothetical factor of proportionality. Projection on the x-axis (multiplying by $\cos(\alpha)$ with the convention that drag is negative)

leads to the formula

$$f^*_{drag} = -D\,2k\,h_0\,|\cos(2kt^*)| \tag{8}$$

and adding this negative force to (7) would yield a theoretical total force $f^*_{thrust} + f^*_{drag}$ in the streamwise x direction.
The flow motion is governed by the Navier–Stokes equations

$$\nabla \cdot \mathbf{u} = 0\,, \qquad \rho\frac{\partial \mathbf{u}}{\partial t} + \rho(\mathbf{u}\cdot\nabla)\mathbf{u} = -\nabla p + \mu\nabla^2\mathbf{u}\,, \tag{9}$$

where $\mathbf{u} = (u, v)$ is the velocity field and p is the pressure, ρ and μ being the constant density and dynamic viscosity. The dimensionless (written with an asterisk) time-dependent pressure force (per unit span) in the fixed coordinate system (x, y) along the heaving foil is

$$\mathbf{f}^* = (f^*_x, f^*_y) = -\frac{1}{\rho U^2_\infty L}\oint (-p)\mathbf{n}\,ds \tag{10}$$

where $\mathbf{n} = (n_x, n_y)$ is the outward unit vector normal to the foil, the integration being performed along the foil's upper and lower face (the minus sign being applied such that a propulsive force is positive, which is the convention generally used). Also, the streamwise component f^*_x will be the key quantity in the forthcoming analysis. At the flow conditions considered, the viscous drag

$$f^*_{\mu,x} = -\frac{1}{\rho U^2_\infty}\oint \mu\left(2\frac{\partial u}{\partial x}n_x + \left(\frac{\partial u}{\partial y} + \frac{\partial v}{\partial y}\right)n_y\right)\,ds \tag{11}$$

(with the minus sign for the drag to be negative) will not contribute significantly to the overall force balance.
In the following, the question will be addressed to which extend the thrust formula (7) and the drag prediction (8) are retrieved in the numerical pressure force data for a heaving foil. Prior to this we summarize in the nest paragraph the numerical environment used for the simulations and we briefly address the numerical convergence issue.

2.1. Numerical procedure and convergence

Direct numerical simulations of equations (9) are performed using the OpenFOAM toolbox (the v1906-version [40]); the solver is inherently three-dimensional and only one void cell is used in the z direction for the present two-dimensional flow setting. The methodology used in OpenFOAM is based on a finite volume discretization of the differential operators together with a mesh-handling using structured or unstructured grids.

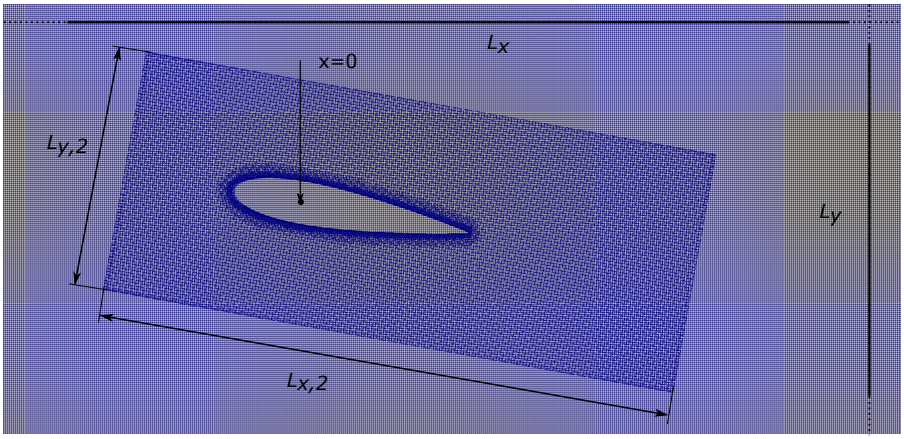


Figure 2: Zoom on the mesh structure, showing the moving overset mesh with dimensions $(L_{x,2}, L_{y,2})$ superimposed to the background mesh with dimensions (L_x, L_y).

The main features of the discretization, based on Gauss' theorem applied to the volume integrals, are briefly summarized. For the approximation of the resulting integrals over the control volume boundaries, the values of the flow quantities at the volume's faces have to be interpolated from the values at the computational nodes. Interpolation practices for finite volume methods are described for instance in [44]. In the forthcoming simulations, for the convective term an upwind interpolation known as upwind differencing scheme is used, where the direction of the flow determines which node provides the cell face value. For the diffusive term a linear interpolation between the faces' two nearest nodes is performed, which is of second order. Linear interpolation is also used for the computation of the gradients normal to the surfaces. Time discretization is based on the first order implicit Euler scheme. In order to deal with the quadratic non-linearity in the Navier-Stokes system, the equations to be solved at each time step are linearized about the result at the previous time step, in the way that the neglected terms are of second order in time, that is smaller than the error of the time discretization. The time step is adapted during the time integration via the Courant number, well known in computational fluid dynamics. All linear systems are solved using the built-in *pimpleFoam* predictor-corrector solver, that merges the PISO and SIMPLE algorithms widely used in computational fluid dynamics [44].
In the present analysis we address large amplitude motions of foils and the so-called overset grid approach (also called Chimera approach) appears to be particularly suitable in this context. This approach consists of meshed subdomains into which the objects are embedded, these meshes being free to move independently one to each other. These subdomains are superim-

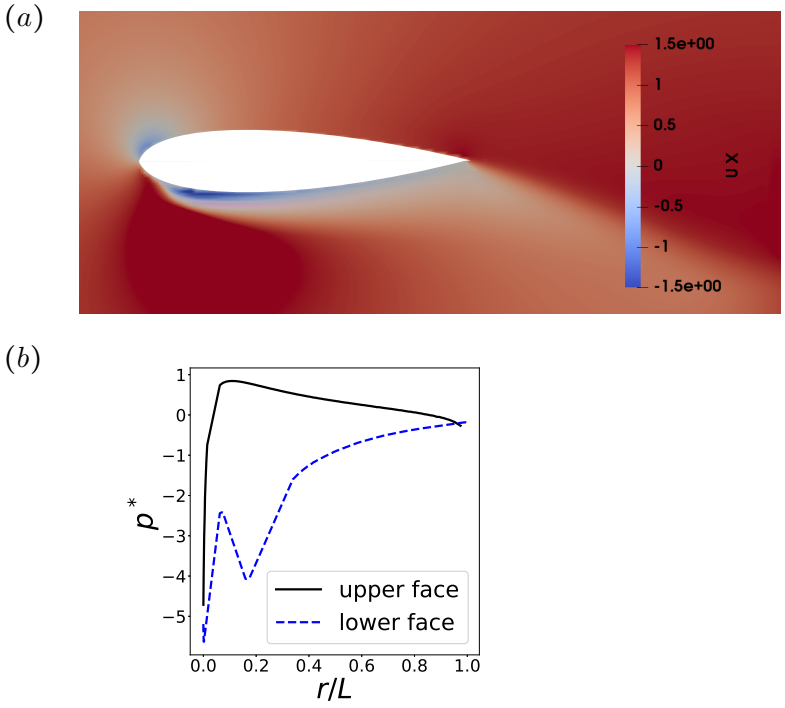


Figure 3: Snapshot of the streamwise velocity component (a) and the corresponding pressure distribution along the upper face and lower face of the foil as function r/L from the leading edge (b). The foil is in the upward motion at approximately the highest heaving velocity. The heaving parameters are k = 0.5 and h_0 = 0.8, the Reynolds number being Re = 5 10^4.

posed to a fixed meshed background domain. For each independent mesh the discretized Navier-Stokes system is advanced in time and at each time step the coupling with the overall solution domain and the background mesh is achieved by transmitting, using interpolation techniques, flow conditions, that is fluxes in the finite volume context used in OpenFOAM. General considerations concerning the coupling of the subdomains can be found in [32] and the use of the Chimera approach in the OpenFOAM-v1906 environment is explained in [41] and [45], for instance. The trajectory of the moving mesh (or independently moving meshes when several moving objects are considered) is prescribed via a text file which is generated prior to the numerical integration of the system. The coordinates in time, with respect to its initial position, of a specific point of the object is to be provided together with the possibility of rotating the object around the axis normal to the computational domain, allowing the combination of translational and pitching motions. The discrete time subdivision of the prescribed motion is to be chosen as small

Options	OpenFOAM v1906, overset, *cellVolumeWeight*, *pimpleFoam*
Reynolds numbers	$5\ 10^4$ ($2.8\ 10^5$ for comparison with experiments)
Velocity boundary and initial conditions	inlet: $\mathbf{u} = U_\infty \mathbf{e}_x$ other boundaries: zero normal gradient initial condition: $\mathbf{u}_0 = U_\infty \mathbf{e}_x$
Pressure boundary conditions	inlet: zero normal gradient other boundaries: zero pressure

Table 1: Main numerical simulation options.

as (or smaller than) the time-step, the value of which being automatically adapted via the Courant number of the Navier-Stokes time integration. In the forthcoming simulations this latter time step is generally of the order of 10^{-3} and the the prescribed motion has been discretized with time-intervals as small as 10^{-4}.

The moving object is here a NACA0018 foil (which is considered in all the simulations) and figure 2 is a zoom showing the overset mesh superimposed to the background mesh (here the position is associated with combined heaving-pitching motion which will be addressed later in this paper). The transmission from the background mesh to the moving mesh is achieved by interpolation (the *cellVolumeWeight* option [41] is used) on the outer border cells of the overset mesh, whereas in return the transmission from the moving mesh back to the background mesh uses the background mesh cells immediately adjacent to the foil's boundary.

For the convergence analysis the Reynolds number $\mathrm{Re} = \rho U_\infty L/\mu$ has been set to $5\ 10^4$. As heaving parameters, the reduced frequency $k = 0.5$ and the heaving amplitude $h_0 = 0.8$ have been chosen, these values being representative of the forthcoming heaving parameter exploration. Uniform free-stream $\mathbf{u} = U_\infty \mathbf{e}_x$ is prescribed at inflow, whereas at the upper and lower boundary zero normal-gradient conditions are imposed for the two components of the flow velocity. A zero pressure is imposed on the boundaries, except at inflow where zero normal-gradient pressure applies. When starting a new computation, uniform free-stream velocity is imposed in the domain as initial condition. The table 1 briefly summarizes the OpenFOAM options and boundary conditions used.

In figure 3 a typical snapshot of the streamwise velocity in the vicinity of the foil is shown, together with the pressure distribution along the upper and lower faces. The foil is in upward motion at a position where the heaving velocity is approximately the maximum, that is the associated angle of attack (see figure 1) is at its maximum, which explains the large separation region

	M_1	M_2	M_3	M_1^+	M_1^{++}
L_x	$[-3L, 7L]$	$[-3L, 7L]$	$[-3L, 7L]$	$[-4.2L, 10L]$	$[-6L, 14L]$
L_y	$[-3L, 3L]$	$[-3L, 3L]$	$[-3L, 3L]$	$[-4.2L, 4.2L]$	$[-6L, 6L]$
$L_{x,2}$	$[-0.7L, 1.7L]$	$[-0.7L, 1.7L]$	$[-0.7L, 1.7L]$	$[-1L, 2.4L]$	$[-1.4L, 3.4L]$
$L_{y,2}$	$[-0.5L, 0.5L]$	$[-0.5L, 0.5L]$	$[-0.5L, 0.5L]$	$[-0.7L, 0.7L]$	$[-1L, 1L]$
Δ_x	$0.01L$	$0.0083L$	$0.0067L$	$0.01L$	$0.01L$
Δ_y	$0.01L$	$0.0083L$	$0.0067L$	$0.01L$	$0.01L$
$\Delta_{x,2}$	$0.016L$	$0.0125L$	$0.01L$	$0.016L$	$0.018L$
$\Delta_{y,2}$	$0.016L$	$0.0125L$	$0.01L$	$0.016L$	$0.018L$
$max(f_x^*)$	0.436	0.408 (-6.4%)	0.427 (4.7%)	0.458 (5%)	0.383 (-12%)

Table 2: Mesh parameters for the computational domain sketched in figure 2. Note that $\Delta_{x,2}$, $\Delta_{y,2}$ are the values in the coarse mesh region of the moving mesh. The last line gives the maximum values of the periodic pressure force f_x^* (taken at $t^* = 3\pi$) for each mesh, the percentage values in parentheses being those of the differences between the value of the finer to the coarser mesh (M_2 to M_1 and M_3 to M_2) and the difference of the values for the larger domains M_1^+ and M_1^{++} with respect to M_1.

at the lower side.

Table 2 lists the parameters for different meshes considered. Here L_x and L_y provide the dimension of the global computational domain with the background mesh. A specific point on the foil at one quarter of the chord from the leading is chosen, which in the forthcoming pitching-heaving motion will be the pitch-pivot point, set at $(x_0, y_0) = (0, 0)$ in the computational domain for the foil at its initial position. For instance $L_x = [-3L, 7L]$ means that the overall length is ten times the foil's chord L, with $3L$ the distance from the inflow boundary to x_0 and $7L$ the distance from x_0 to the outflow boundary. The vertical dimension $L_y = [-3L, 3L]$ means a domain's height of $6L$ with a distance $3L$ from the foil's chord line to the bottom as well as to the top. The dimensions of the moving overset-mesh are given by $L_{x,2}$ and $L_{y,2}$ respectively (see figure 2). Furthermore Δ_x, Δ_y (respectively $\Delta_{x,2}, \Delta_{y,2}$) are the grid sizes in both directions, for the background and moving mesh, respectively. While for each domain the background mesh has a constant grid size, on the moving mesh, when approaching the foil, two successive refinements are performed in a transient zone, dividing the grid size by 4. At last, in the very vicinity of the foil and inside the boundary layer three additional refinements are performed, dividing again the grid size by 8.

The meshes labeled M_1, M_2, M_3 correspond to the same domain size, but to successive grid-size refinements by an almost constant factor (as advocated for instance in [46]), the grid size being divided here two times by ≈ 1.25. The meshes labeled M_1, M_1^+ and M_1^{++} in table 2 have the same density of dis-

cretization (besides a somewhat coarser grid in the moving domain for mesh M_1^{++}), the domain sizes being successively increased by a factor of $\approx \sqrt{2}$.
Considering for instance the mesh labeled M_2, the grid size of the background mesh is $(\Delta x, \Delta y) = (0.0083L, 0.0083L)$. In the coarse mesh region of the moving mesh the values are $(\Delta_{x,2}, \Delta_{y,2}) = (0.0125L, 0.0125L)$ which is refined to $(\Delta_{x,2}/32, \Delta_{y,2}/32)$, yielding a grid size as small as $0.0004L$ in the boundary layer region. Concerning the numerical resolution in the vicinity of the foil, the Blasius formula $5L\sqrt{r/L}\sqrt{1/\mathrm{Re}}$ for the boundary-layer thickness (r/L being the dimensionless distance from the leading edge) could provide an idea about the number of grid points inside the boundary-layer region. This formula yields $0.022L\sqrt{r/L}$ and given the grid size $0.0004L$ close to the foil, one may estimate that roughly $55\sqrt{r/L}$ points are inside the boundary layer (that is still 10 points at a dimensionless distance r/L as small as 0.033 from the leading edge). It should also be mentioned that the background mesh has to be chosen sufficiently fine to ensure a reliable transmission of the flow conditions from the moving mesh. Indeed, the discrete contour associated with the background mesh cells the closest to the foil must fit in the best possible way with the foil's contour.
The pressure forces generated by the foil's motion is at the heart of the investigation and we focus on this quantity for numerical validation. The dynamic force (10) computed for different meshes are superimposed in figure 4(a) and the curves are seen to be very close one to each other, besides slight differences at the peak values. The viscous drag (11) has been computed as well and is depicted in figure 4(b) (for two meshes only, the curves being close) and it is interesting to note that (after a short transient) at $t^\star = \pi, 2\pi...$ the viscous force peak is positive, given that the heaving velocity $\dot{h}^\star = 2kh_0\cos(t^\star)$ (for $k = 0.5$) undergoes a minimum or maximum, leading to large separation of the flow field alternately on the upper face and lower face. Note that the drag force is almost two orders of magnitude smaller than the pressure force, what justifies to only consider the pressure force for thrust calculations, at least for this range of Reynolds numbers.
After a short transient regime the dynamic pressure becomes periodic with peaks at $t^\star = \pi, 2\pi...$ (see figure 4(a)) and for the convergence analysis, table 2 provides the maximum value of $f_x^\star$ (taken at $t^\star = 3\pi$) for each mesh. The differences, expressed in percentage, between these values when performing successive grid refinement, that is for M_2 compared to M_1 and M_3 compared to M_2, are provided as well. The differences slightly decrease and change sign, which indicates oscillatory convergence (see for instance [46] for general considerations on validation and verification of numerical simulation results). Concerning the influence of the computational domain size, the val-

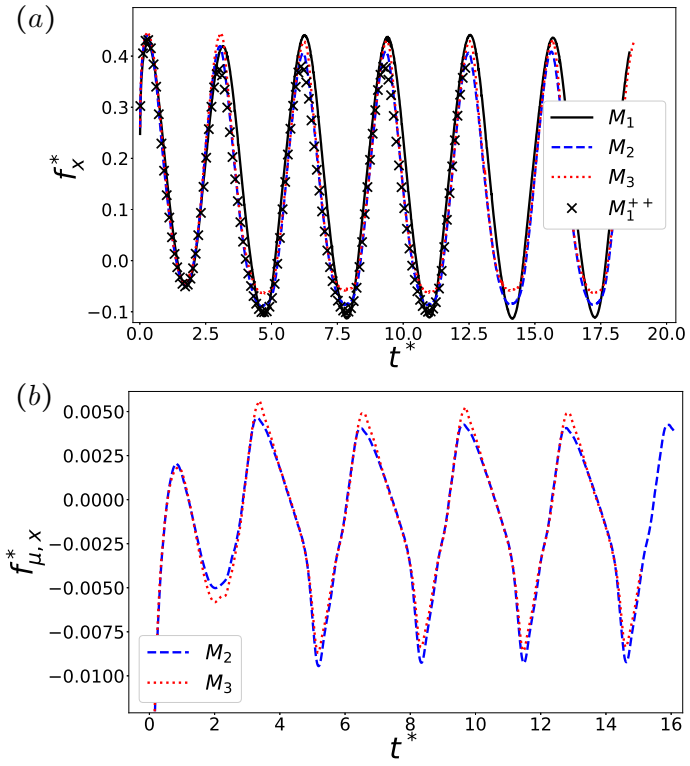


Figure 4: Streamwise component f_x^* of the pressure force (a) and viscous drag (b) as function of time t^* and for different meshes (for the mesh-labels M_1, M_2, M_3, M_1^{++} see table 2), for a heaving amplitude $h_0 = 0.8$ and frequency $k = 0.5$, at $\mathrm{Re} = 5\,10^4$.

ues for M_1^+ and to M_1^{++} are compared to the value for M_1, the pressure peak being higher for M_1^+ and lower for M_1^{++}. It is not surprising that finite-size effects are observed, the differences remaining however relatively small. It has to be emphasized that a definite mesh convergence evidence is hardly to be achieved, for this unsteady flow field. Indeed, as mentioned earlier for instance the time step is automatically adapted via the Courant number and it hence changes when refining the grid. Also, when enlarging the domains' dimensions, the relative size between the moving domain and the background domain has been kept constant, which modifies however the distance from the foil to the domains' interpolation region.
Note that the background mesh for the M_2 discretization contains a bit more than $8.7\,10^5$ points and the moving mesh about $2\,10^4$ points (due to the refining close to the foil) which yields a total number of almost $9\,10^5$ points. This M_2 mesh has been chosen in all the forthcoming simulations, as a compromise between precision and computational cost.

2.2. Thrust scaling

The formula (7) for lift-induced thrust has been derived according to classical fluid mechanics, the underlying hypotheses being slender body and potential flow theory as well as small angles of attack. When considering for instance cycloidal propulsion, the foils' rotation can be decomposed into heaving and surging, the heaving and surging amplitude being likely of the same order than the foils' chord length (in such devices the foils undergo in general also additional pitching motions). For instance, the Voith Schneider propulsion addressed in [47] would correspond to $h_0 = 0.75$ whereas the reduced frequency k is of order one and the angle of attack (2) experienced by the heaving foil takes values during a heaving period as large as 50°. The question is whether a formula such as (7) is meaningful for the heaving NACA0018 foil considered here.

Numerical data have been generated for frequencies $k = 0.25, 0.5, 0.75, 1$, the heaving amplitudes being $h_0 = 0.4, 0.6, 0.8, 1$, that is 16 (k, h_0) parameter combinations have been considered, the Reynolds number being $\mathrm{Re} = 5\ 10^4$. Of course, the Reynolds number associated with real propulsion in water would at least be one or two orders of magnitude higher. The value considered is however likely to be large enough for the pressure stress computations to provide significant thrust results, viscous effects being negligible for the force outcome at this Reynolds number.

The oscillatory pressure force f_x^* can be decomposed as

$$f_x^* = f_{l,x}^* + f_{d,x}^* \tag{12}$$

with $f_{l,x}^*$ the lift force and $f_{d,x}^*$ the drag force, both projected on the x-axis. For the comparison with the formula (7) and (8), the factors of proportionality C and D have to be estimated. The choice has been made that the time-averaged values $\langle f_{l,x}^* \rangle$ and $\langle f_{d,x}^* \rangle$ ($\langle \cdot \rangle$ being the average over one heaving period) coincide with those of the formula and given that $\langle \cos^2(2kt^*) \rangle = 1/2$ and $\langle |\cos(2kt^*)| \rangle = 2/\pi$, C and D have been chosen such that

$$\langle f_{l,x}^* \rangle = C\ 2\pi k^2 h_0^2, \quad \langle f_{d,x}^* \rangle = -D\ \frac{4}{\pi} k h_0, \tag{13}$$

C and D having been computed for all the heaving parameter combinations. The figures 5 and 6 show the computed thrust and drag contributions to the pressure force over several heaving periods, for the heaving parameter $k = 0.5, h_0 = 0.8$ as well as $k = 0.75, h_0 = 0.6$, respectively. The theoretical formula (7) and (8) are superimposed. The corresponding proportionality factors are $C = 0.477, D = 0.728$ and $C = 0.419, D = 0.637$, respectively, computed according to (13). It is seen that the formulas are representative of the

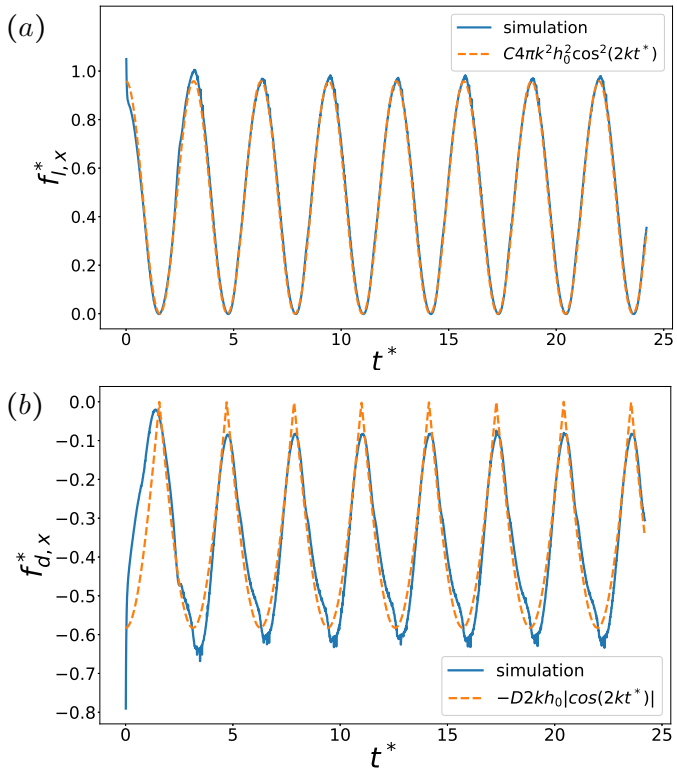


Figure 5: Dimensionless lift-induced thrust $f^*_{l,x}$ (a) and pressure drag $f^*_{d,x}$ (b) as function of time t^*, for a heaving amplitude $h_0 = 0.8$ and frequency $k = 0.5$, at Re = 5 10^4. The theoretical formulas $f^*_{thrust} = C\ 4\pi k^2 h_0^2 \cos^2(2kt^*)$ and $f^*_{drag} = -D\ 2kh_0|\cos(2kt^*)|$ are superimposed as the broken lines, for $C = 0.477, D = 0.728$.

computed dynamic thrust and drag, but it has to be emphasized that different C, D values are retrieved. Considering the 16 parameter combinations, it appears that C varies between 0.3 and 0.6, whereas the D coefficients are in an even larger range from 0.3 to 1.2.
Assuming a linear dependence of these coefficients with respect to k and h_0, writing

$$C(k, h_0) = c_1 + c_2 k + c_3 h_0, \quad D(k, h_0) = d_1 + d_2 k + d_3 h_0, \tag{14}$$

the coefficients

$$(c_1, c_2, c_3) = (0.745, -0.277, -0.150), \quad (d_1, d_2, d_3) = (-0.387, 0.640, 0.923) \tag{15}$$

have been obtained performing a least-square fit with the 16 values of C and D as given by the computations for the 16 parameter configurations considered. Note that $C(k, h_0)$ and $D(k, h0)$ are always positive in the parameter

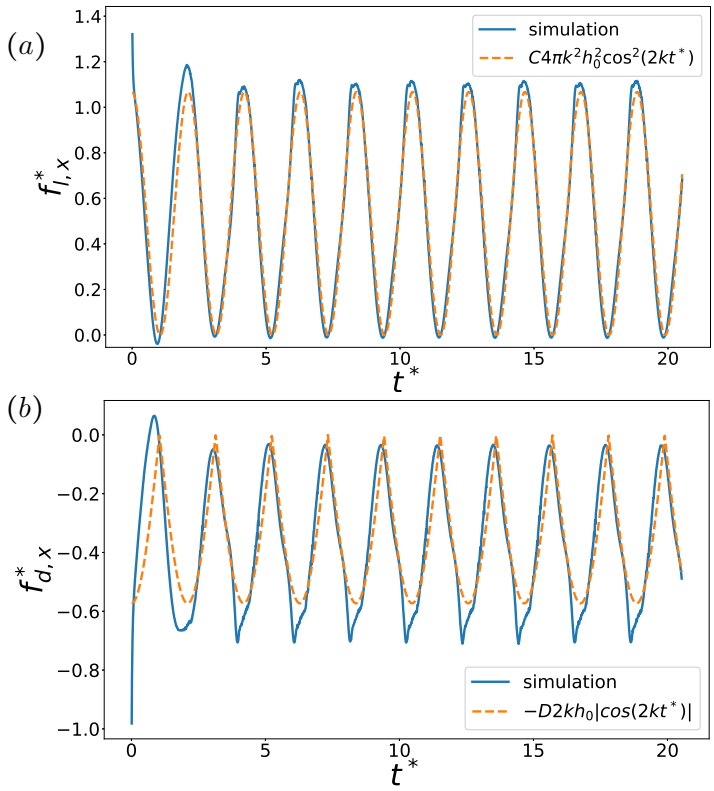


Figure 6: Dimensionless lift-induced thrust $f^*_{l,x}$ (a) and pressure drag $f^*_{d,x}$ (b) as function of time t^*, for a heaving amplitude $h_0 = 0.6$ and frequency $k = 0.75$, at Re = 5 10^4. The theoretical formulas $f^*_{thrust} = C\ 4\pi k^2 h_0^2 \cos^2(2kt^*)$ and $f^*_{drag} = -D\ 2kh_0|\cos(2kt^*)|$ are superimposed as the broken line, for $C = 0.419, D = 0.637$.

range. The theoretical model for the mean pressure force is accordingly

$$F^*_{theory} = 2\pi C(k, h_0)k^2 h_0^2 - \frac{4}{\pi} D(k, h_0)kh_0 \tag{16}$$

(with $C(k, h_0)$ and $D(k, h_0)$ given by 14). The time-average F^*_x of the oscillatory pressure force (12) has been computed and the values are shown in figure (7) against its model counterpart; it is seen that the theoretical thrust prediction is close to the computed values. Note that classical thrust coefficient formula have been derived in [7] for small heaving amplitudes, based on potential flow formulas [48], for an idealized airfoil represented as a straight line, that is without pressure form drag. This theory yields a formula $2\pi k^2 h_0^2(F^2 + G^2)$, known as Garrick's theory where F and G are function of the reduced frequency tabulated in [7]. The corresponding thrust values have for instance been compared in [11] with numerical values (obtained with a two-dimensional panel code) for plunging NACA foils, however for h_0 values smaller than 0.4 which is the lowest value considered here.

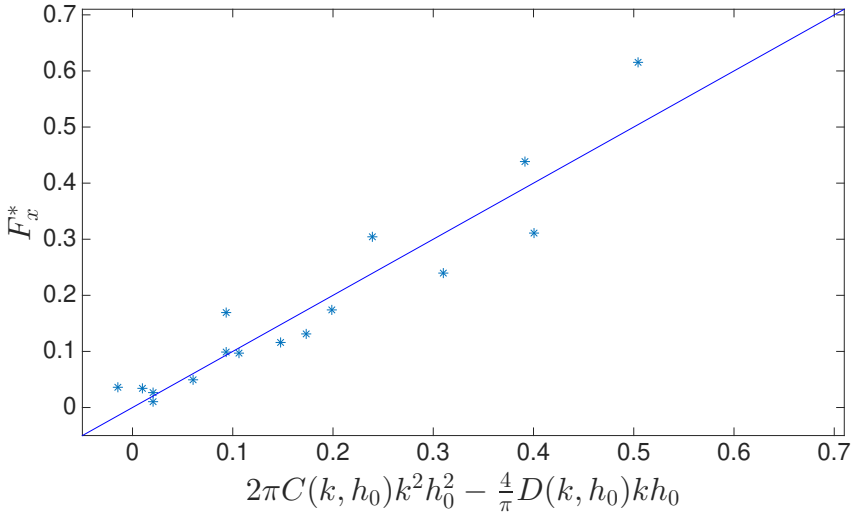


Figure 7: Time averaged pressure force F_x^* against its model counterpart (16), the symbols representing the values for the 16 parameter values (k, h_0), with $k = 0.25, 0.5, 0.75, 1$ and $h_0 = 0.4, 0.6, 0.8, 1$, the solid line being the bisector of the first quadrant angle.

It is interesting to note that the thrust part in the model (16) is at least roughly of the order of magnitude with what one gets with Garrick's formula: it has been checked that for the (k, h_0) combinations considered, the latter formula would however provide values about 20% to 40% higher. Large amplitude oscillations have also been experimentally addressed in [25], considering the Strouhal number formed with the maximum foil excursion $2Lh_0$, that is $St = 2fLh_0/U_\infty$, as dimensionless frequency. It is easily seen that $St = 2kh_0/\pi$ and in [25] some evidence is provided for a thrust dependence on St^2 (that is $\sim k^2h_0^2$). The present investigation however suggests that such a simplified law only provides a rough estimate of the thrust performance.

3. Heaving-pitching foil

In order to put a step forward towards the modeling of propulsion devices, a pitching motion is superimposed to the heaving motion considered so far. The pitching motion considered has the same period as the heaving motion, introducing a phase-shift ϕ such that the pitching angle is

$$\theta(t^*) = \alpha_0 \sin(2kt^* + \phi), \tag{17}$$

(the heaving motion being $h^*(t) = h_0 \sin(2kt^*)$). The pitch-pivot point is set at one quarter of the foil's chord from the leading edge, that is the chord-line from the pivot point to the trailing edge forms an angle $\theta(t^*)$ with the

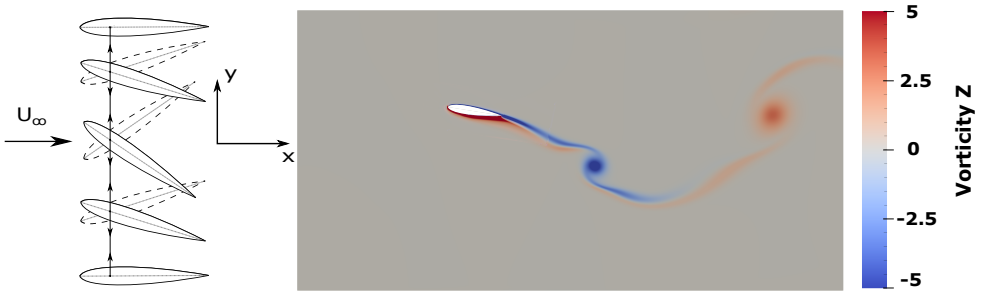


Figure 8: Sketch (left) of the heaving-pitching foil, in its upward motion (solid contour) and downward motion (broken contour). The snapshot (right) is the vorticity field for the parameters $(k, h_0, \alpha_0) = (0.5, 0.8, 20°)$, the foil being in its upward motion at $\theta(t) \approx -0.5\,\alpha_0$ and $h^*(t) \approx 0.866\,h_0$.

horizontal inflow direction. The phase-shift $\phi = -\pi/2$ has been chosen and accordingly $\theta(t^*) = -\alpha_0 \cos(2kt^*))$, which corresponds to the foil's motion in an experimental device to be discussed in the next section.
Simulations have been performed for three values of the maximum pitching angle, that is $\alpha_0 = 10°,\ 20°,\ 30°$, again at Re = 5 10^4. The left picture in figure 8 shows a sketch of the foils position during the upward and downward heaving motion. An instantaneous flow vorticity field for the pitching angle $\alpha_0 = 20°$, the heaving amplitude $h_0 = 0.8$ and the reduced frequency $k = 0.5$ is shown as well, the foil being in its upward heaving motion at the instant such that $\theta(t) \approx -0.5\,\alpha_0$ and $h^*(t) \approx 0.866\,h_0$. For the same heaving amplitude $h_0 = 0.8$ and frequency $k = 0.5$, the oscillatory pressure force f_x^* is shown for the three pitching angles in figure 9(a). As can be seen, the maximum peak is for $\alpha_0 = 10°$, the result for $\alpha_0 = 20°$ is close to the values for pure heaving, whereas the thrust performance is the lowest for the highest pitching angle $\alpha_0 = 30°$. For these parameter values the viscous force $f_{\mu,x}^*$ in the x-direction associated with the viscous stress has been computed as well and it is shown in figure 9(b). It is interesting to note that while for $\alpha = 0, 10°$ the peak at $t^* = \pi, 2\pi...$ is positive, for higher pitching angles however it is negative. This can be explained by the fact, that when the foil is pitching with a phase shift $-\pi/2$ with respect to the heaving motion, the apparent incoming flow direction sketched in figure 1 forms, when pitching is added, an angle $\alpha(t) - \theta(t)$ with the chord line. This means that the pitching lowers the angle of attack experienced by the foil and hence the intensity of separation. In all cases the mean viscous force is of course negative, contributing as drag. Note gain that the magnitude of viscous drag is negligible with regard to the thrust. In the previous section it has been attempted to scale the dynamic force in terms of the reduced frequency k and the heaving amplitude h_0 and

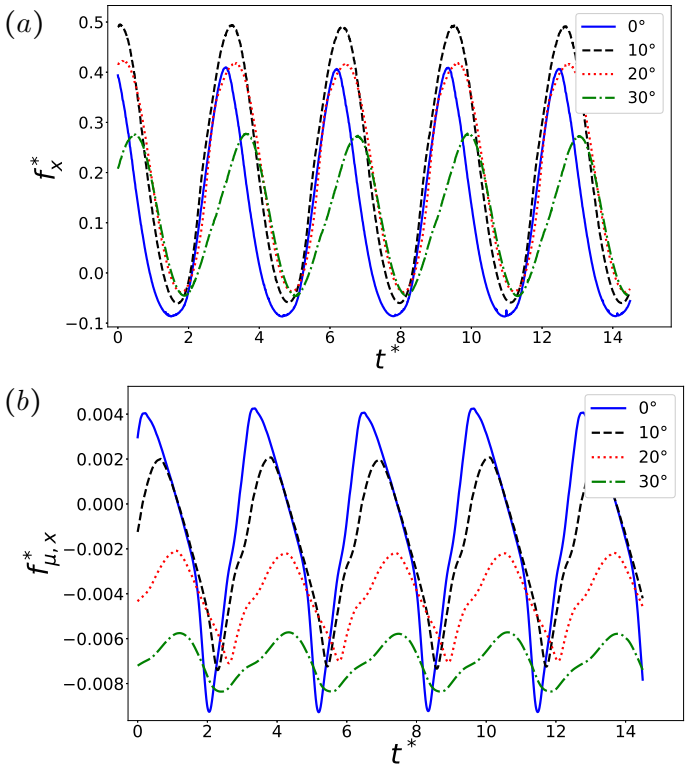


Figure 9: Oscillatory pressure force f_x^* (a) and viscous force $f_{\mu,x}^*$ (b) for the foil undergoing heaving-pitching motion, for the frequency $k = 0.5$, heaving amplitude $h_0 = 0.8$ and four different pitching angles $\alpha_0 = 0, 10°, 20°, 30°$.

the model (16) proved to fit to some degree the time-dependent thrust force as well as its time-averaged values. Adding pitching to the heaving motion, it may be conjectured that the induced force is a combination of a contribution due to heaving as well as one associated with pitching, together with a coupling component.

Pure pitching motions for a plate with vanishing thickness has been considered in [13] for relatively small pitching angles and it could be shown that in terms of reduced frequency and maximum pitching angle α_0 the time-averaged thrust scales scales as

$$a\,\alpha_0^2 k^2 + b\,\alpha_0^2 k, \tag{18}$$

a and b being coefficients depending on the pitch-pivot point location. Note that a similar scaling has been proposed for instance in [16]. When adding the pitching to the heaving motion, the outward unit vector normal to the foil rotates with respect to the vertical axis $\mathbf{e}_y$ by the pitching angle θ. The resulting acceleration of the fluid in the x-direction may hence be estimated

to be $\ddot{h}\sin(\theta)$. Note that $\frac{L}{U_\infty^2}\ddot{h} = -4k^2h_0\sin(2kt^*)$, given the expression (1) of the heaving motion, and the pressure force in dimensionless form associated with this acceleration is proportional to

$$k^2h_0\sin(2kt^*)\sin(\alpha_0\sin(2kt^* + \phi)), \tag{19}$$

given the expression (17). Even though the pitching's maximum angle α_0 is not particularly small, one is nevertheless tempted to consider the expression above at the leading order in α_0 which would yield by taking the time-average an expression proportional to $k^2h_0\alpha_0$. While the proportionality factor will probably depend on the the phase shift ϕ of the pitching motion with respect to heaving, there is however no reason that it may be inferred from the time average of the product $\sin(2kt^*)\sin(2kt^* + \phi)$ (which would be zero for instance for $\phi = -\pi/2$ considered here). Indeed, the fluid-foil dynamics by itself is likely to introduce phase shifts between the periodic foil motion and the induced flow acceleration.

In the previous section, the time-dependent pressure induced by the pure heaving motion could be reasonably fitted for the set of parameter values considered and the law (16) could be derived for the time-averaged force as the sum of lift-induced thrust and drag, with however non constant coefficients given by (14). At leading order in the parameters, the lift-induced thrust is proportional to $k^2h_0^2$, whereas the drag is proportional to kh_0. Retaining these leading order terms, adding terms proportional to $\alpha_0^2k^2$ and α_0^2k (associated with the pitching law (18)) as well as a term proportional to $k^2h_0\alpha_0$ which stands for the force component due to the coupling between pitching and the heaving acceleration, the following time averaged pressure force expression

$$F^*_{theory} = B_1\alpha_0^2k^2 + B_2\alpha_0^2k + B_3k^2h_0^2 + B_4kh_0 + B_5\alpha_0k^2h_0 \tag{20}$$

is proposed.

The coefficients $B_j, j = 1, \cdots, 5$ have been computed by a least-square fit for the 36 parameter values considered, that is all the (α_0, k, h_0) combinations (with $\alpha_0 = 10°, 20°, 30°$, $k = 0.25, 0.5, 0.75, 1$ and $h_0 = 0.6, 0.8, 1$). The values found are

$$B_1 = -0.9165, B_2 = -1.5409, B_3 = 0.6431, B_4 = 0.0496, B_5 = 2.4108 \tag{21}$$

and the computed force F_x^* against its model counterpart (20) is shown in figure 10. It is seen that the model fits well for the range of parameter values considered, where small heaving amplitudes or large frequencies are discarded. As already mentioned, the parameter values are however in the range of an experimental cycloidal propulsion device discussed in the next section.

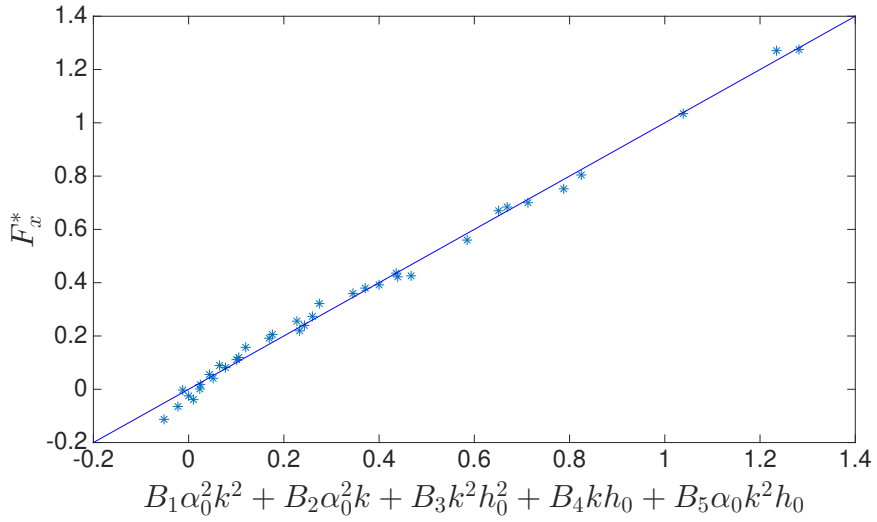


Figure 10: Time averaged pressure force F_x^* against its model counterpart (20), with coefficients (21), the symbols representing the values for the 36 parameter values (α_0, k, h_0), with $\alpha_0 = 10°, 20°, 30°$, $k = 0.25, 0.5, 0.75, 1$ and $h_0 = 0.6, 0.8, 1$; the solid line is the bisector of the first quadrant angle.

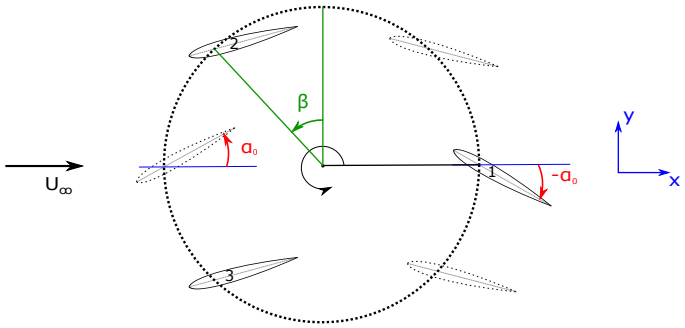


Figure 11: Sketch of the experimental cycloidal propulsion device designed by the Naval Academy Research Institute in France. Three NACA0018 foils labeled $1, 2, 3$ rotate in a circular motion around an axis. The foils' trajectory is marked as the circle, the angle between two foils being 120°. The foils sketched with solid contours are at their positions at t_0 (when foil 1 has the highest pitching amplitude α_0) and the hatched contours indicate their positions $T/6$ later, T being the period of rotation.

4. Application to cycloidal propulsion

The most widely known cycloidal propulsion device is the Voith-Schneider propeller the performance of which has for instance been numerically addressed in [47]. These type of propellers consist of several blades rotating around a vertical axis, the individual plates themselves undergoing pitching motions around their own pivot points. These propulsion devices are capa-

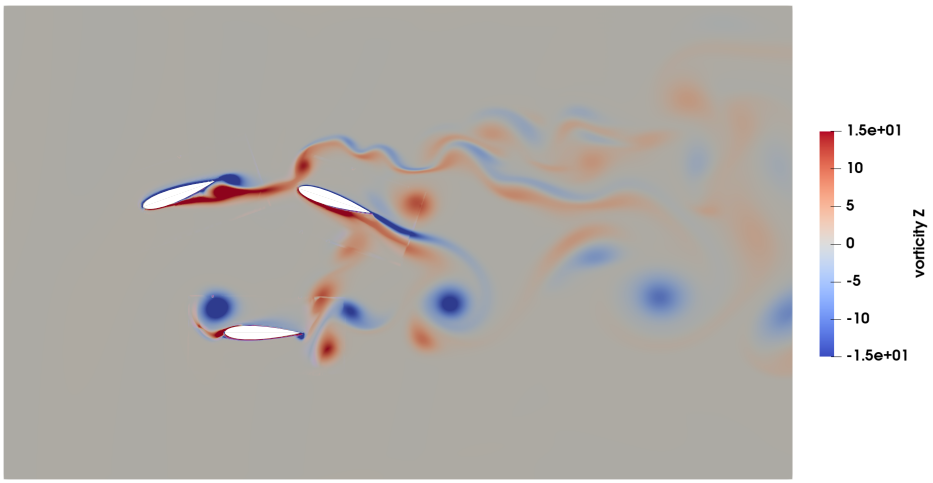


Figure 12: Snapshot of the vorticity field for three rotating and pitching foils, for the parameter values $h_0 = 1.143$, $k = 0.6$ and $\alpha_0 = 22°$. This configuration corresponds to that sketched in figure 11, the Reynolds number being $\mathrm{Re} = 5\ 10^4$.

ble to generate thrust forces in all directions. They are very efficient when maneuverability is required and are hence frequently used for the propulsion of tugs and ferries, for instance. A cross-flow propeller has recently been subject of experimental investigations at the Naval Academy Research Institute (IRENav) in France, where such a device has been designed, the pitching motions being controlled electrically by servo-motors enslaved by the main motor ([42]), numerical simulations having been performed for this configuration too [49]. The device with three foils is sketched in figure 11, where the solid foils' contours are at their positions at t_0 when foil labeled 1 has the highest pitching amplitude α_0. The circle drawn corresponds to the trajectory of the foil and the hatched foils' contours stand for their respective positions at $t_0 + T/6$. The angle between two foils is 120°. The pitch-pivot point is at $L/4$ from the leading edge, the incoming flow arriving from the left.

The configuration, for which measurements have been performed using Ifremer facilities at Boulogne-sur-Mer, is that of a NACA0018 foil with chord length $L = 0.35\ m$, whereas the radius of the circle of motion is $R = 0.4\ m$. The period of circular rotation and pitching is the same for each foil and the motion can be decomposed into heaving, pitching and a surge motion parallel to the x-direction of incoming flow. The motions are synchronizes such that the dimensionless heaving motion h^* and surge motion s^* are

$$h^* = h_0 \sin(2kt^*), \quad s^* = h_0 \cos(2kt^*) \tag{22}$$

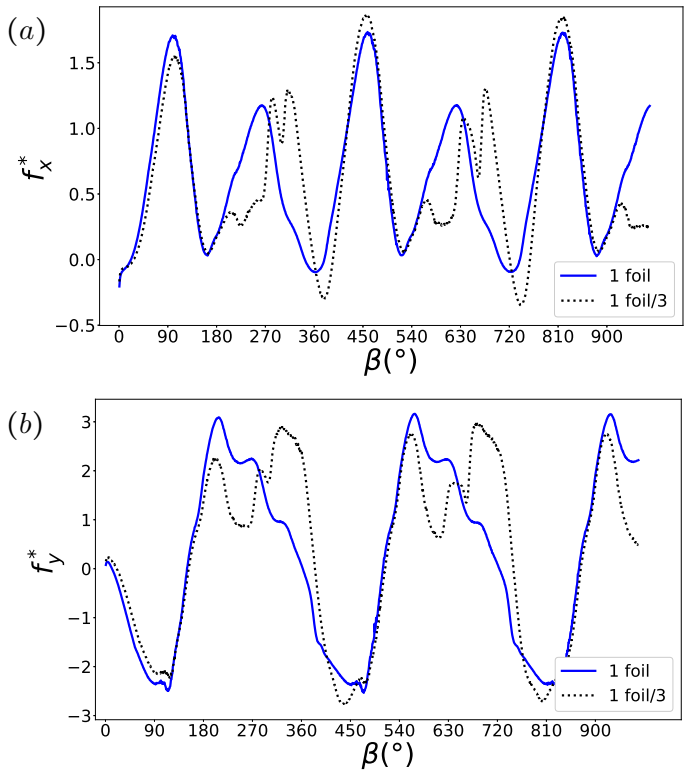


Figure 13: Comparison between the pressure force for one pitching-rotating foil and the pressure force around one foil pitching and rotating together with two others. Component in the x-direction (a) and in the y-direction (b), as function of angle β (by convention, $\beta = 0°, 360°, ...$ is the highest vertical position for the successive periods of rotation, see figure 11). The parameters are $k = 0.6, h_0 = 1.143, \alpha_0 = 22°$.

(h^* being the distance from the axis's center in the vertical direction y and s^* the distance in the horizontal direction x). The pitching angle around the individual pivot points is

$$\theta(t) = -\alpha_0 \cos(2kt^*). \tag{23}$$

that is the phase shift with the heaving motion is $-\pi/2$ as in the previous section. The position of foil labeled 1 in figure 11 would correspond to $t^* = n\pi/k$ (with n an integer).

In the experimental investigation the incoming flow velocity is of the order of 1 m/s in the Ifremer water tank which yields a Reynolds number (based on the foil's chord) of the order of $3.5\ 10^5$. The dimensionless heaving amplitude is $h_0 = R/L = 1.143$, the reduced frequencies considered varying between $k = 0.25$ and $k = 0.45$. The pitching angle α_0 range is between 10° and 40°. Besides the Reynolds number, which in the present simulations is $\mathrm{Re} = 5\ 10^4$,

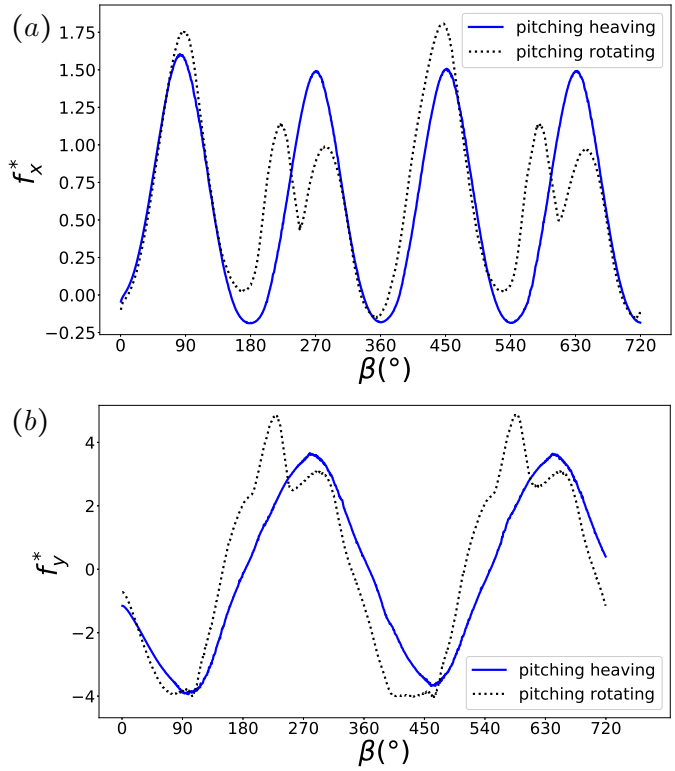


Figure 14: Comparison between the pressure force for one pitching-heaving foil and for a pitching-rotating foil. Component in the x-direction (a) and in the y-direction (b), as function of angle β (by convention, $\beta = 0°, 360°, ...$ is the highest vertical position for the successive periods of rotation, see figure 11). The parameters are $k = 0.5, h_0 = 1, \alpha_0 = 10°$.

these parameters are within the range of those considered in the previous section for the heaving-pitching foil. In section 2, for the pure heaving motion, the influence of the mesh as well as the size of the computational domain has been assessed for this latter Reynolds number and the mesh labeled M_2 (for a computational domain $10L$ in the x-direction and $6L$ in the y-direction) proved appropriate to get reliable force results.
Simulations have been performed for these mesh parameters, at Re = 5 10^4 and considering the complete configuration with the three rotating foils, with $h_0 = 1.143$, $\alpha_0 = 22°$ and $k = 0.6$. A snapshot of the flow field is shown in figure 12. The question naturally arises to what extent the force generated by one foil rotating with the two others differs from what one would get for a single foil in an equivalent rotating motion. This comparison has been performed for the same parameter values $h_0 = 1.143$, $\alpha_0 = 22°$ $k = 0.6$ as those corresponding to the snapshot in figure 12. The results are plotted as function of angle β, $\beta = 0, 360°...$ being the maximal vertical position (see

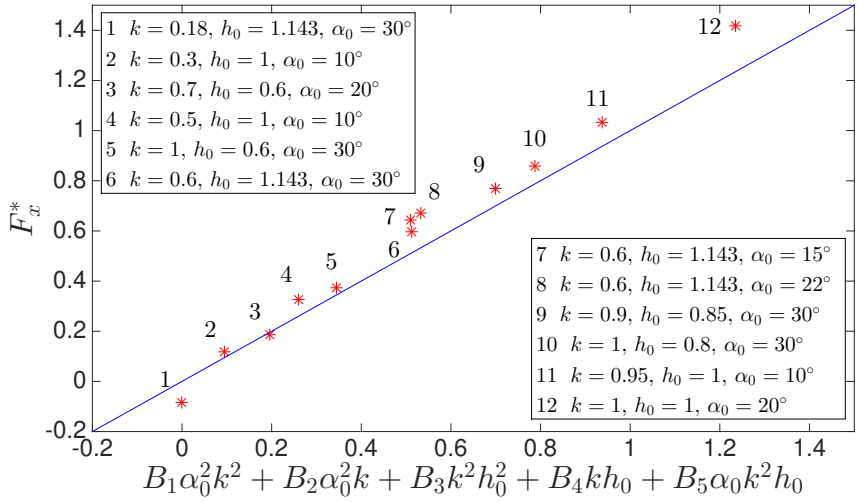


Figure 15: Time averaged pressure force F_x^* are shown as the symbols for a pitching-rotating foil against its model counterpart (20) for pitching-heaving foil with coefficients $B_j, j = 1, \cdots, 5$ given by (21). The solid line being the bisector of the first quadrant angle.

figure 11) of the foil around which the pressure force is computed. It is seen that when the foil's trajectory is on the left semicircle ($0 < \beta < 180°$) the pressure force components in the x direction almost superimpose, whether a single rotating foil is considered or a foil in the device. As expected, when the foil's trajectory crosses the wake structure of the device (at the right semicircle of the trajectory) the peaks of the pressure force are somewhat shifted between the two configuration. On the whole however, and at least for a rotation radius h_0 close to one, the results are rather close and in particular when time-averages are considered. This supports the idea that to some degree the thrust for one single rotating flow may be extrapolated to recover the global thrust for a configuration like that in figure 11 (by superimposing three times the oscillatory pressure force for one foil with shifts of 120° in angle β).

The rotating-pitching foil differs from the heaving-pitching foil by the additional horizontal back and forth motion and the question is to what degree this latter surge motion affects the thrust results. The oscillatory pressure force for a single heaving-pitching foil and a rotating-pitching foil has been computed, for different parameter combinations. The result for $k = 0.5, h_0 = 1, \alpha_0 = 10°$ is shown in figure 14, the two force components being depicted as function of β (it is recalled that $\beta = 0°, 360°...$ are the highest vertical position for each period). The curves are close, the force in the x direction exhibiting however a somewhat higher peak when the rotating foil

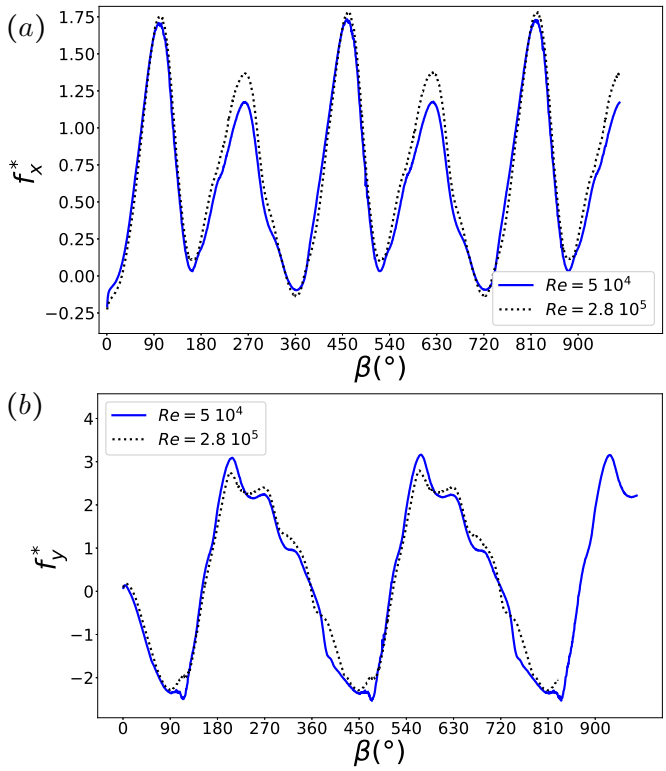


Figure 16: Comparison between the pressure force components in the x-direction (a) and y-direction (b), at two different Reynolds numbers Re = 5 10^4 and Re = 2.8 10^5, for one pitching-rotating foil for the parameter values $k = 0.6$, $h_0 = 1.143$, $\alpha = 22°$.

moves toward the incoming flow, and a lower peak when moving in the opposite direction. One may wonder whether the heaving-pitching force model (20) may still be relevant when rotation instead of heaving is considered. The time-averaged thrust force for the rotating and pitching foil has been computed for 6 parameter combinations and the values are compared with this thrust law in figure 15. The computed values are shown as the symbols and it is seen that the model prediction is still rather reliable, which means that in average the additional surging motion does not contribute significantly to the global force.

For the experimental device at IRENav, measurements have not be performed at a Reynolds number of 5 10^4, but for instance at Re = 2.8 10^5, that is for an incoming flow velocity of 0.8 m/s in a water tank, the blades' chord being 0.35 m. Of course, to perform the numerical simulation at such a high Reynolds number is questionable, even in the two-dimensional case, at least if one aims at capturing complex flow structures. Concerning the pressure force at the heart of the present investigation, it is however conjectured that

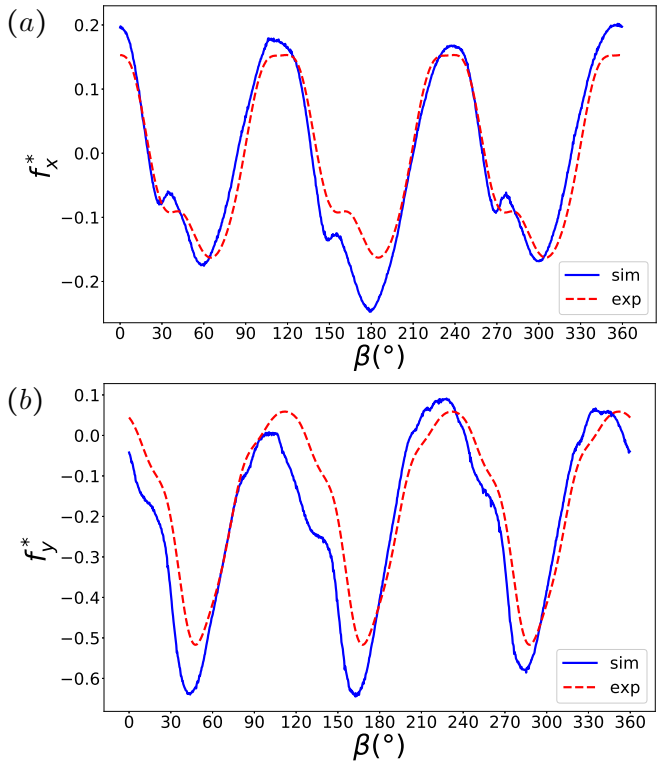


Figure 17: Comparison between measurements for the cycloidal device and the simulation results: pressure component in the x-direction (a) and in the y-direction (b), at Re = 2.8 10^5, with pitching angle $\alpha_0 = 30°$ and frequency $k = 0.29$. The dimensionless radius of the circular trajectory is $h_0 = 1.143$. The results for one period of rotation is shown, $\beta = 0$ corresponding to the instant when one of the three foils is at the top (cf. figure 11).

it is not strongly affected by the Reynolds number (the value 5 10^4 considered so far being already in a relatively high Reynolds number range). To give some evidence for this assumption, for the same computational mesh M_2 as used so far, the oscillatory pressure force of one rotating-pitching foil has been computed for Re = 2.8 10^5 and the comparison with the result at Re = 5 10^4 is shown in figure 16, for $k = 0.6$ and $h_0 = 1.143$ (this latter amplitude is that of the experimental device). It is seen that the thrust values $f_x^\star$ are rather close, besides a slightly stiffer peak for the high Reynolds number case at the most downstream position (with respect to the incoming flow) of the foil on its circular trajectory (at $\beta = 270°, 630°...$).
In the experimental thrust performance investigation at the Boulogne-sur-Mer Ifremer facilities, the time-dependent hydrodynamic loads are measured with a blade embedded load cell. Note that the blades have a rather large span-to-chord aspect ratio of 2.8 and three-dimensional effects are possibly

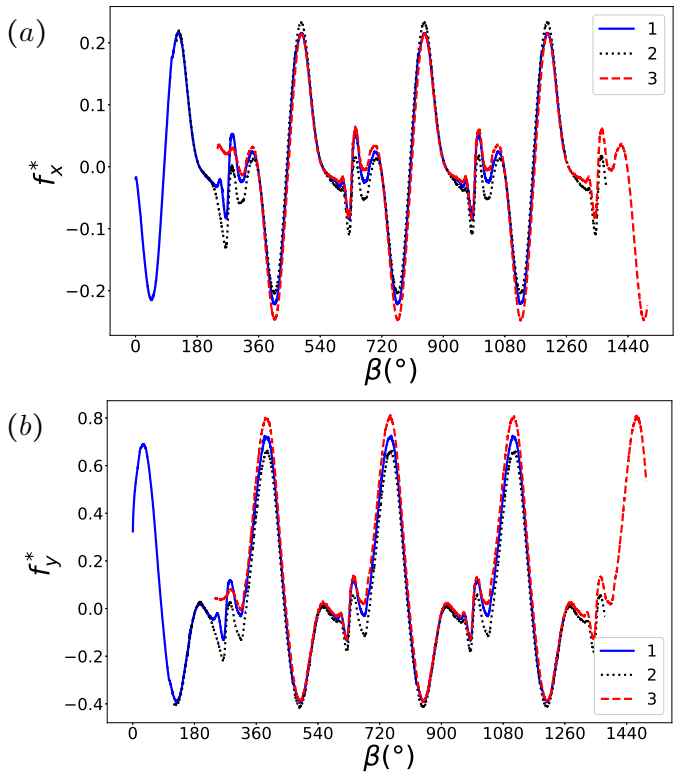


Figure 18: Computed individual force values f_x^* (a) and f_y^* (b), for each blade (labeled $1, 2, 3$) in the device, $\beta = 0°, 360°, \cdots$ corresponding to the highest vertical position of the individual blade's trajectory (four periods of rotation are shown). The parameters are the same as in figure 17.

limited regarding the overall thrust generated by each foil. A detailed description of the experimental propeller design is given in [42]. The hydrodynamic force is measured on one blade and the total force is reconstructed by shifting the loads by respectively 120° and 240°, which means that the reconstructed total force is $T/3$ periodic with T the period of rotation.

The flow structure generated by the rotating plates might however not exhibit exactly this $T/3$-periodicity. In the numerical simulation the instantaneous force values for each blade have been computed and added to form the total force. Measurements for a pitching angle $\alpha_0 = 30°$ have been performed and figure 17 shows the comparison with the simulation results, for both the force components, at $k = 0.29$. It is seen that the results coincide fairly well, but the $T/3$ periodicity, or equivalently the 120° periodicity, is not exactly observed in the numerical simulation results. Indeed, the individual force values depicted in figure 18 for each blade do not exactly coincide at identical positions ($\beta = 0°, 360° \cdots$ being the highest vertical position, four rotation periods

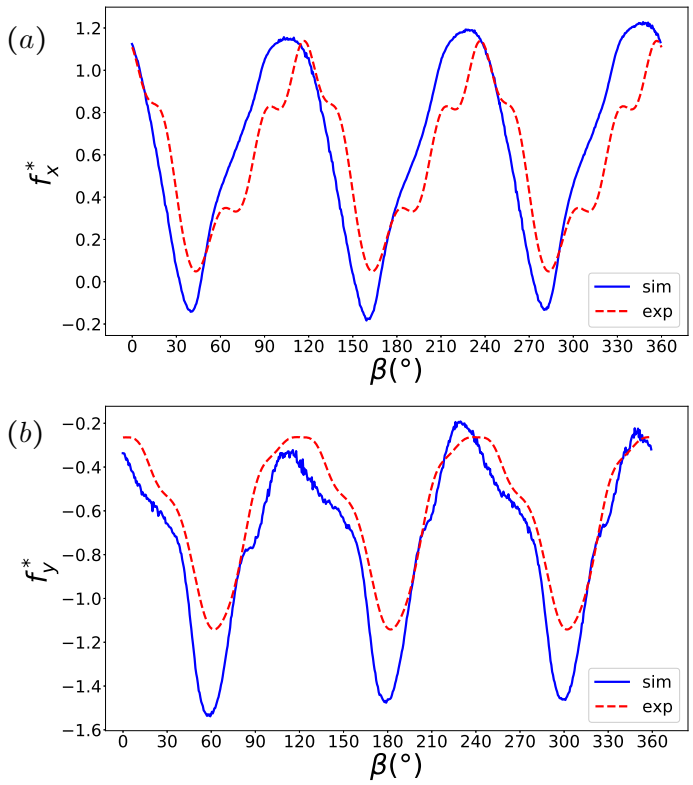


Figure 19: Comparison between measurements for the cycloidal device and the simulation results: pressure component in the x-direction (a) and in the y-direction (b), at Re = $2.8\,10^5$, with pitching angle $\alpha_0 = 30°$ and frequency $k = 0.49$. The dimensionless radius of the circular trajectory is $h_0 = 1.143$. The results for one period of rotation is shown, $\beta = 0$ corresponding to the instant when one of the three foils is at the top (cf. figure 11).

being shown), in particular in the downstream half of the circular trajectory. This is to be attributed to slightly different flow structures encountered by the individual plates at identical positions.

The comparison between the measurements and the simulations at the higher frequency $k = 0.49$ is shown in figure 19. Now, the simulation results are not far from exhibiting a $T/3$ period: for this frequency the curves differ a little more, but the general trends are however retrieved in the simulations. Regarding the time-averaged values, for the frequency $k = 0.29$ one finds $F_x^* = -0.0094$ in the experiment whereas the simulation result is $F_x^* = -0.0118$. At the higher frequency $k = 0.49$, one gets $F_x^* = 0.6008$ and $F_x^* = 0.6359$ for the measurements and the simulations, respectively, thus the measured dynamic forces as well as the time averaged quantities are approximately retrieved in the numerical simulations.

5. Concluding discussion

The present investigation has shown that the overset-option and the general modelization capabilities of OpenFOAM are suitable for the simulation of a rigid structure undergoing large scale motions in an incoming flow field. The advantage of such a body-fitted mesh approach is to provide accurately the dynamic forces generated in this system. A theoretical model, which proved reliable for the time-dependent pressure stress as well as for the global time averaged thrust, could be derived for a heaving foil in the form

$$F^*_{theory} = 2\pi C(k,h_0)k^2h_0^2 - \frac{4}{\pi}D(k,h_0)kh_0.$$

The first term of the right-hand side is associated with the lift-induced thrust, the second term standing for form-drag due to a virtual angle of attack during the heaving motion. The expressions $C(k,h_0)$ and $D(k,h_0)$ could not reliably be taken as constants, but rather as linear functions of the heaving amplitude h_0 and the reduced frequency k. A scaling for the thrust merely proportional to $k^2h_0^2$, as proposed for instance in [25], should hence be used with caution.

The present investigation has been guided by the objective to numerically simulate fluid-structure interactions for motions associated with cycloidal propulsion. For pitching-heaving motions and focusing on time-averaged thrust prediction, a theoretical scaling (20) is proposed. Besides the $k^2h_0^2$ and kh_0 terms of heaving, the expressions $\alpha_0^2k^2$ and α_0^2k associated to pitching (see [13, 16]) enter, as well as the coupling term $\alpha_0k^2h_0$. This law with 5 scaling parameters has been proven to fit with the numerical simulation data, as shown in figure 10. It appears that this law is still reliable when adding a surging motion, or equivalently, when addressing pitching-rotating foils typical for cross-flow propellers, at least for the simulation data at a Reynolds number of $5\ 10^4$. The experimental device designed at the IRENav operates however at higher Reynolds numbers, but still below those of industrial devices. Also, this cycloidal propulsion device has a plate's span-to-chord aspect ratio of 2.8 and the resulting quasi-two-dimensional measurements have been shown to be in good agreement with the two-dimensional simulations, for the same Reynolds number $\mathrm{Re} = 2.8\ 10^5$ as in the experiment.

The values (21) for the proportional parameters $B_1,\cdots,B_5$ of the thrust law (20) have been computed by least-square fit with numerical simulation data at $\mathrm{Re} = 5\ 10^4$ and for a pitching-heaving foil. Addressing in this concluding discussion briefly the reliability of the law for pitching-rotating motions when changing the Reynolds number, figure 20 depicts the time-averaged pressure force at three different Reynolds numbers $\mathrm{Re} = 10^4, 5\ 10^4, 2.8\ 10^5$,

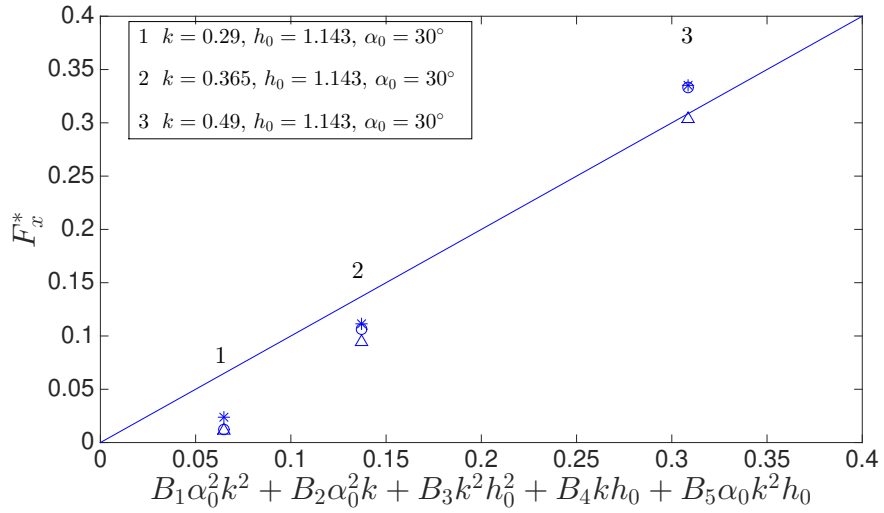


Figure 20: Time averaged pressure force F_x^* are shown as the symbols for a pitching-rotating foil against its model counterpart (20) for pitching-heaving foil with coefficients $B_j, j = 1, \cdots, 5$ given by (21), at Re = 10^4 ($*$); Re = 5 10^4 ($\triangle$) and Re = 2.8 10^5 ($\circ$). The solid line being the bisector of the first quadrant angle.

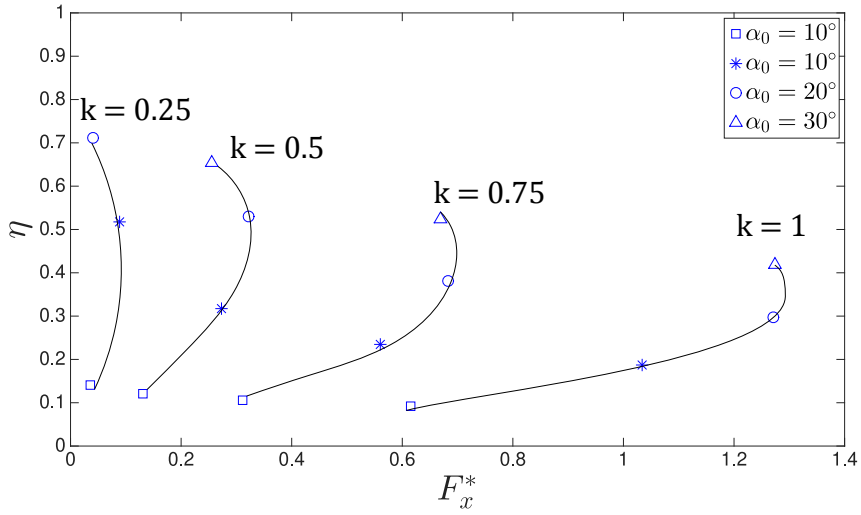


Figure 21: Efficiency parameter η computed as the formula (24) versus thrust F_x^*, for different pitching-heaving parameters with h_0 = 1. The symbols represent the different pitching angles and the solid curves are line-fits through the values at the different frequencies k. The Reynolds number of the computations is Re = 5 10^4.

for h_0 = 1.143 corresponding to the experimental device and for α_0 = 30° (the three frequencies chosen being in the parameter range of the experimen-

tal measurements). The computed force values are relatively close to the law and they only slightly differ with the Reynolds number, at least for this motion-parameter range.

One may conjecture that a law such as (20) might be helpful, in the sense that typical pitching-rotation parameters may be inferred for particular thrust regimes, such as zero thrust for a given flow velocity or maximum thrust, for instance. It has to be emphasized that of course the proportional parameters $B_1, \cdots, B_5$ in (20) will depend on the specific foils considered (here a NACA0018 profile, which was used in the experimental device) and more importantly on the phase-shift between the pitching and rotating motions.

Of course, the propulsive efficiency also plays an important role for the performance of moving foils. This efficiency is in general measured by the ratio of thrust power output to the power input to the foil. The time-averaged power input for a heaving-pitching foil is $P_i = \langle f_y \dot{h} \rangle + \langle m_z \dot{\theta} \rangle$ (e.g. [14], [16]), with m_z the moment about the pitch-pivot point and f_y the pressure force in the direction of heaving motion. The efficiency can be written as the ratio of dimensionless quantities and one gets the expression for the present foil's motion with a phase shift $-\pi/2$ between the pitching and heaving

$$\eta = \frac{F_x^*}{\langle h_0 \, f_y^* \, 2k \, \cos(2kt^*) \rangle + \langle \alpha_0 \, m_z^* \, 2k \, \sin(2kt^*) \rangle}. \tag{24}$$

Figure 21 shows the efficiency η as function of thrust F_x^*, the different solid curves being line-fits at constant k through the values for different pitching angles (the heaving amplitude is set to $h_0 = 1$). It is seen that for a given frequency k the efficiency is the lowest for pure heaving ($\alpha_0 = 0$) and it increases with the pitching angle. Efficiency of relatively large amplitude heaving and pitching foils has been addressed for instance in [25], these authors pointing out discrepancies in the literature concerning efficiency measurements. The present computations provide efficiency values in the range between 0.1 and 0.7. The issue of the present investigation was thrust-prediction and a detailed efficiency analysis is not attempted. One may however remark that the efficiency globally decreases with the frequency (for a fixed heaving amplitude) which is in general line with the measurements reported in [25]. In this latter investigation the phase shift between pitching and heaving is $\phi = 3\pi/2$ which means that in this case the pitching increases the angle of attack associated with the heaving motion. In our case however (that is for a phase shift $\phi = -\pi/2$) the angle of attack decreases with pitching (see section 3). Therefore, the fact that the efficiency in the present case increases with the angle of pitching corresponds to the known fact that large angles of attack are detrimental to efficiency (see [25]). Finally, it can be inferred from figure 21 that while thrust globally increases with the oscillation frequency,

there is however for each k-value an optimal (with regard to thrust) pitching angle.

Acknowledgment

Centre de Calcul Intensif d'Aix-Marseille is acknowledged for granting access to its high performance computing resources.

References

[1] M. S. Triantafyllou, F. S. Hover, A. H. Techet, D. K. Yue, Review of hydrodynamic scaling laws in aquatic locomotion and fishlike swimming, Appl. Mech. Rev. 58 (2005) 226–237. doi:10.1115/1.1943433.

[2] T. Von Kármán, J. Burgers, Aerodynamic Theory: General aerodynamic theory : Perfect fluids / [By] Th. von Kármán ; J. M. Burgers, no. vol. 2, J. Springer, 1943.

[3] M. M. Koochesfahani, Vortical patterns in the wake of an oscillating airfoil, AIAA J. 27 (1989) 1200–1205. doi:10.2514/3.10246.

[4] D. G. Bohl, M. M. Koochesfahani, Mtv measurements of the vortical field in the wake of an airfoil oscillating at high reduced frequency, J. Fluid Mech. 620 (2009) 63–88.

[5] J. Moubogha Moubogha, U. Ehrenstein, J. A. Astolfi, Forces on a pitching plate: an experimental and numerical study, Appl. Ocean Res. 69 (2017) 27–37. doi:10.1016/j.apor.2017.09.003.

[6] P. Brousseau, M. Benaouicha, S. Guillou, Fluid-structure interaction effects on the deformable and pitching plate dynamics in a fluid flow, Applied Ocean Research 113 (2021) 102720. doi:10.1016/j.apor.2021.102720.

[7] I. E. Garrick, Propulsion of a flapping and oscillating airfoil, Langley Memorial Aeronautical Lab. Rept. 567, Langley Field, VA, 1936.

[8] T. Y. Wu, Swimming of a waving plate, J. Fluid Mech. 10 (1961) 321–344. doi:10.1017/S0022112061000949.

[9] S. Ramananarivo, R. Godoy-Diana, B. Thiria, Passive elastic mechanism to mimic fish-muscle action in anguilliform swimming, J. R. Soc. Interface 10 (2013) 20130667. doi:10.1098/rsif.2013.0667.

[10] M. Piñeirua, R. Godoy-Diana, B. Thiria, Resistive thrust production can be as crucial as added mass mechanisms for inertial undulatory swimmers, Phys. Rev. E 92 (2015) 021001(R). doi:10.1103/PhysRevE.92.021001.

[11] K. D. Jones, M. Platzer, Numerical computation of flapping-wing propulsion and power extraction, in: 35th AIAA Aerospace Sciences Meeting, AIAA Paper 97-0826, 1997.

[12] K. Moored, D. Quinn, Inviscid scaling laws of a self-propelled pitching airfoil, AIAA J. 57 (2019) 3686–3700. doi:10.2514/1.J056634.

[13] J. Labasse, U. Ehrenstein, P. Meliga, Numerical exploration of the pitching plate parameter space with application to thrust scaling, Appl. Ocean Res. 101 (2020) 102278. doi:10.1060/j.apor.2020.102278.

[14] A. W. Mackowski, C. H. K. Williamson, Direct measurement of thrust and efficiency of an airfoil undergoing pure pitching, J. Fluid Mech. 765 (2015) 524–543. doi:10.1017/jfm.2014.748.

[15] J. M. Anderson, K. Streitlien, D. S. Barrett, M. S. Triantafyllou, Oscillating foils of high propulsive efficiency, J. Fluid Mech. 360 (1998) 41–72. doi:10.1017/S0022112097008392.

[16] D. Floryan, T. Van Buren, C. W. Rowley, A. J. Smits, Scaling the propulsive performance of heaving and pitching foils, J. Fluid Mech. 822 (2017) 386–397. doi:10.1017/jfm.2017.302.

[17] X. Wu, X. Zhang, X. Tian, X. Li, W. Lu, A review on fluid dynamics of flapping foils, Ocean Eng. 195 (2020) 1–30. doi:10.1016/j.oceaneng.2019.106712.

[18] S. Abbaszadeh, S. Hoerner, T. Maître, R. Leidhold, Experimental investigation of an optimised pitch control for a verti cal-axis turbine, IET Renewable Power Generation 13 (2019) 3106–3112. doi:10.1049/iet-rpg.2019.0309.

[19] J. Bartels, D. Jürgens, The voith schneider propeller: current applications and new developments, in: Heidenheim: Voith Publication, 2006.

[20] J. O. Scherer, Experimental and theoretical investigation of large amplitude oscillating foil propulsion systems, HYDRONAUTICS, Incorporated, Technical Report 662-1, 1968.

[21] J. Hu, T. Li, C. Guo, Two-dimensional simulation of the hydrodynamic performance of a cycloidal propeller, Ocean Engineering 217 (2020) 107819. doi:10.1016/j.oceaneng.2020.107819.

[22] A. Halder, C. Walther, M. Benedict, Hydrodynamic modeling and experimental validation of a cycloidal propeller, Ocean Engineering 154 (2018) 94–105. doi:10.1016/j.oceaneng.2017.12.069.

[23] B. Paillard, J. A. Astolfi, F. Hauville, Uranse simulation of an active variable-pitch cross-flow darrieus tidal turbine: Sinusoidal pitch function investigation, International Journal of Marine Energy 11 (2015) 9–26. doi:10.1016/j.ijome.2015.03.001.

[24] M. G. Chopra, Large amplitude lunate-tail theory of fish locomotion, J. Fluid Mech. 74 (1976) 161–182. doi:10.1017/S0022112076001742.

[25] D. Floryan, T. Van Buren, A. J. Smits, Large-amplitude oscillations of foils for efficient propulsion, Phys. Rev. Fluids 4 (2019) 093102. doi:10.1103/PhysRevFluids.4.093102.

[26] C. S. Peskin, Flow patterns around heart valves: a numerical method, J. Comput. Phys. 10 (1972) 252–271. doi:10.1016/0021-9991(72)90065-4.

[27] A. Pinelli, I. Z. Naqavi, U. Piomelli, J. Favier, Immersed-boundary methods for general finite-difference and finite-volume navier-stokes solvers, J. Comp. Phys. 229 (2010) 9073–9091. doi:10.1016/j.cp.2010.08.021.

[28] A. Goza, T. Colonius, A strongly-coupled immersed-boundary formulation for thin elastic strucures, J. Comp. Phys. 336 (2017) 401–411. doi:10.1016/j.cp.2017.02.027.

[29] B. Kallemov, A. Bhalla, B. E. Griffith, A. Donev, An immersed boundary method for rigid bodies, Comm. Appl. Math. Comput. Sci. 11 (2016) 79–141. doi:10.2140/camcos.2016.11.79.

[30] J. Steger, J. Benek, On the use of composite grid schemes in computational aerodynamics, Computer Methods in Applied Mechanics and Engineering 64 (1987) 301–320. doi:10.1016/0045-7825(87)90045-4.

[31] H. S. Tang, S. C. Jones, F. Sotiropoulos, An overset-grid method for 3d unsteady incompressible flows, Journal of Computational Physics 191 (2003) 567–600. doi:10.1016/S0021-9991(03)00331-0.

[32] G. G. Houzeaux, B. Eguzkitza, R. Aubry, H. Owen, M. Vázquez, A chimera method for the incompressible navier-stokes equations, International Journal for Numerical Methods in Fluids 75 (2014) 155–188. doi:10.1002/fld.3886.

[33] B. Roget, J. Sitaraman, Robust and efficient overset grid assembly for partitioned unstructured meshes, Journal of Computational Physics 260 (2014) 1–24. doi:10.1016/j.jcp.2013.12.021.

[34] H. Ye, D. Wan, Benchmark computations for flows around a stationary cylinder with high reynolds numbers by rans-overset grid approach, Applied Ocean Research 65 (2017) 315–326. doi:10.1016/j.apor.2016.10.010.

[35] G. R. Tabor, M. H. Baba-Ahmadi, Inlet conditions for large eddy simulation: A review, Comp. Fluids 39 (2010) 553–567. doi:10.1016/j.compfluid.2009.10.007.

[36] M. Meldi, M. V. Salvetti, P. Sagaut, Quantification of errors in large-eddy simulations of a spatially evolving mixing layer using polynomial chaos, Phys. Fluids 24 (2012) 035101. doi:10.1063/1.3688135.

[37] D. A. Lysenko, I. S. Ertesvåg, K. E. Rian, Modeling of turbulent separated flows using OpenFOAM, Comp. Fluids 80 (2013) 408–422. doi:10.1016/j.compfluid.2012.01.015.

[38] L. Gao, J. Xu, G. Gao, Numerical simulation of turbulent flow past airfoils on OpenFOAM, Procedia Eng. 31 (2012) 756–761. doi:10.1016/j.proeng.2012.01.1098.

[39] B. Selma, M. Désilets, P. Proulx, Optimization of an industrial heat exchanger using an open-source cfd code, Appl. Therm. Eng. 69 (2014) 241–250. doi:10.1016/j.applthermaleng.2013.11.054.

[40] https://www.openfoam.com/news/main-news/openfoam-v1906, 2019.

[41] P. Tisovska, Description of the overset mesh approach in esi version of openfoam, in: Proceedings of CFD with OpenSource Software, 2019, Edited by Nilsson H., 2019. doi:10.17196/OS_CFD#YEAR_2019.

[42] G. Fasse, F. Becker, F. Hauville, J.-A. Astolfi, G. Germain, An experimental blade-controlled platform for the design of smart cross-flow propeller, Ocean Engineering 250 (2022) 110921. doi:10.1016/j.oceaneng.2022.110921.

[43] G. K. Batchelor, An Introduction to Fluid Dynamics, Cambridge University Press, 1967.

[44] J. Ferziger, M. Perić, Computational Methods for Fluid Dynamics, 3rd edition, Springer, 2002.

[45] D. D. J. Chandar, On overset interpolation strategies and conservation on unstructured grids in openfoam, Computer Physics Communications 239 (2019) 72–83. doi:10.1016/j.cpc.2019.01.009.

[46] R. V. Wilson, F. Stern, H. W. Coleman, E. G. Paterson, Comprehensive approach to verification and validation of cfd simulations-part2: application for rans simulation of a cargo/container ship, Journal of Fluids Engineering 123 (2001) 803–810. doi:10.1115/1.1412236.

[47] E. Esmailian, H. Ghassemi, S. A. Heidari, Numerical investigation of the performance of voith schneider propulsion, American Journal of Marine Science 2 (2014) 58–62. doi:10.12691/marine-2-3-3.

[48] T. Theodorson, Genneral theory of aerodynamic instability and the mechanism of flutter, NACA TR 498, 1935.

[49] G. Fasse, A. Bayeul-Lainé, O. Coutier-Delgosha, A. Curutchet, B. Paillard, F. Hauville, Numerical study of a sinusoidal transverse propeller, in: IOP Conference Series:Earth and Environmental Science, IOP Publishing, 2019, p. 052007.